

Geophysical Research Letters

RESEARCH LETTER

10.1029/2019GL084123

Key Points:

- Rift and icefront icequakes were identified
- Icefront icequakes are most frequent during the austral summer when swell forcing is greatest in the absence of sea ice
- An empirical ocean-to-ice shelf displacement transfer function is obtained

Supporting Information:

- Supporting Information S1
- Movie S1
- Movie S2
- Movie S3

Correspondence to:

Z. Chen,
zhc012@ucsd.edu

Citation:

Chen, Z., Bromirski, P., D., Gerstoft, P., Stephen, R. A., Lee, W. S., Yun, S., et al. (2019). Ross Ice Shelf icequakes associated with ocean gravity wave activity. *Geophysical Research Letters*, 46, 8893–8902. <https://doi.org/10.1029/2019GL084123>

Received 14 JUN 2019

Accepted 29 JUL 2019

Accepted article online 1 AUG 2019

Published online 9 AUG 2019

Corrected 28 OCT 2019

This article was corrected on 28 OCT 2019. See the end of the full text for details.

Ross Ice Shelf Icequakes Associated With Ocean Gravity Wave Activity

Z. Chen¹, P. D. Bromirski¹, P. Gerstoft¹, R. A. Stephen², W. S. Lee³, S. Yun³, S. D. Olinger⁴, R. C. Aster⁵, D. A. Wiens⁶, and A. A. Nyblade⁷

¹Scripps Institution of Oceanography, University of California, San Diego, La Jolla, CA, USA, ²Woods Hole Oceanographic Institution, Woods Hole, MA, USA, ³Korea Polar Research Institute, Incheon, South Korea, ⁴Department of Earth and Planetary Sciences, Harvard University, Cambridge, MA, USA, ⁵Department of Geosciences, Colorado State University, Fort Collins, CO, USA, ⁶Department of Earth and Planetary Sciences, Washington University in St. Louis, St. Louis, MO, USA, ⁷Department of Geosciences, Pennsylvania State University, University Park, PA, USA

Abstract Gravity waves impacting ice shelves illicit a suite of responses that can affect ice shelf integrity. Broadband seismometers deployed on the Ross Ice Shelf, complemented by a near-icefront seafloor hydrophone, establish the association of strong icequake activity with ocean gravity wave amplitudes (A_G) below 0.04 Hz. The Ross Ice Shelf-front seismic vertical displacement amplitudes (A_{SV}) are well correlated with A_G , allowing estimating the frequency-dependent transfer function from gravity wave amplitude to icefront vertical displacement amplitude ($T_{GSV}(f)$). $T_{GSV}(f)$ is 0.6–0.7 at 0.001–0.01 Hz but decreases rapidly at higher frequencies. Seismicity of strong icequakes exhibits spatial and seasonal associations with different gravity wave frequency bands, with the strongest icequakes observed at the icefront primarily during the austral summer when sea ice is minimal and swell impacts are strongest.

1. Introduction

Ice shelves play an important role in restraining the grounded ice discharge to the sea (MacAyeal, 1987; Rignot et al., 2004; Scambos et al., 2004). Their integrity is thus crucial in moderating sea level rise. Ocean forcing can impact ice shelf integrity both thermally and dynamically. Although internal glaciological stresses may be the dominant driving force of crevasse formation and expansion (Bassis et al., 2008), surface and basal melting can facilitate this process by thinning the ice and providing additional pressure in fissures (Scambos et al., 2000). Experiments on the Ross Ice Shelf (RIS) suggest that stress perturbations induced by ocean gravity waves (Lipovsky, 2018) and tides (Olinger et al., 2019) may also contribute to ice fracture and rift propagation, further reducing ice shelf integrity. Persistent gravity wave forcing with intermittent strong impacts, including swell, infragravity (IG) waves, and tsunami (Bromirski et al., 2010, 2017; Chen et al., 2018), may fatigue ice shelves, promote iceberg calving (Brunt et al., 2011), and potentially trigger the collapse of weakened ice shelves (Massom et al., 2018).

Classical studies model an ice shelf response to gravity wave impacts as a floating plate of uniform thickness (Fox & Squire, 1991; Papanastasiou et al., 2019; Press & Ewing, 1951). Recent studies include two-dimensional (Ilyas et al., 2018; Sergienko, 2010) and three-dimensional (Sergienko, 2017) finite-element simulations and estimates of extensional stress induced by flexural and extensional waves from in situ seismic data (Lipovsky, 2018). Such simulations indicate that induced dynamic stress strongly depends on the system geometry, including ice shelf thickness and physical properties, subshelf cavity thickness, and bathymetry, each having significant uncertainty and spatial variability not adequately accounted for. Models are potentially capable of estimating the ocean-to-ice shelf transfer function, which can be compared with the empirical estimates presented here.

To understand ice shelf dynamics associated with the response to gravity wave forcing and to provide observations to validate ice shelf modeling efforts, a 34-station broadband seismic array was deployed on the RIS from October 2014 to November 2016, with three stations 2 km from the ice front (Bromirski et al., 2015). Each seismic station includes a three-component Nanometrics T120 PHQ seismometer, buried 1 m below the surface, with sampling rates of 1 and 200 Hz. Additionally, a three-component Nanometrics Trillium Compact broadband ocean bottom seismometer system with a HighTech HTI-04-PCA/ULF hydrophone

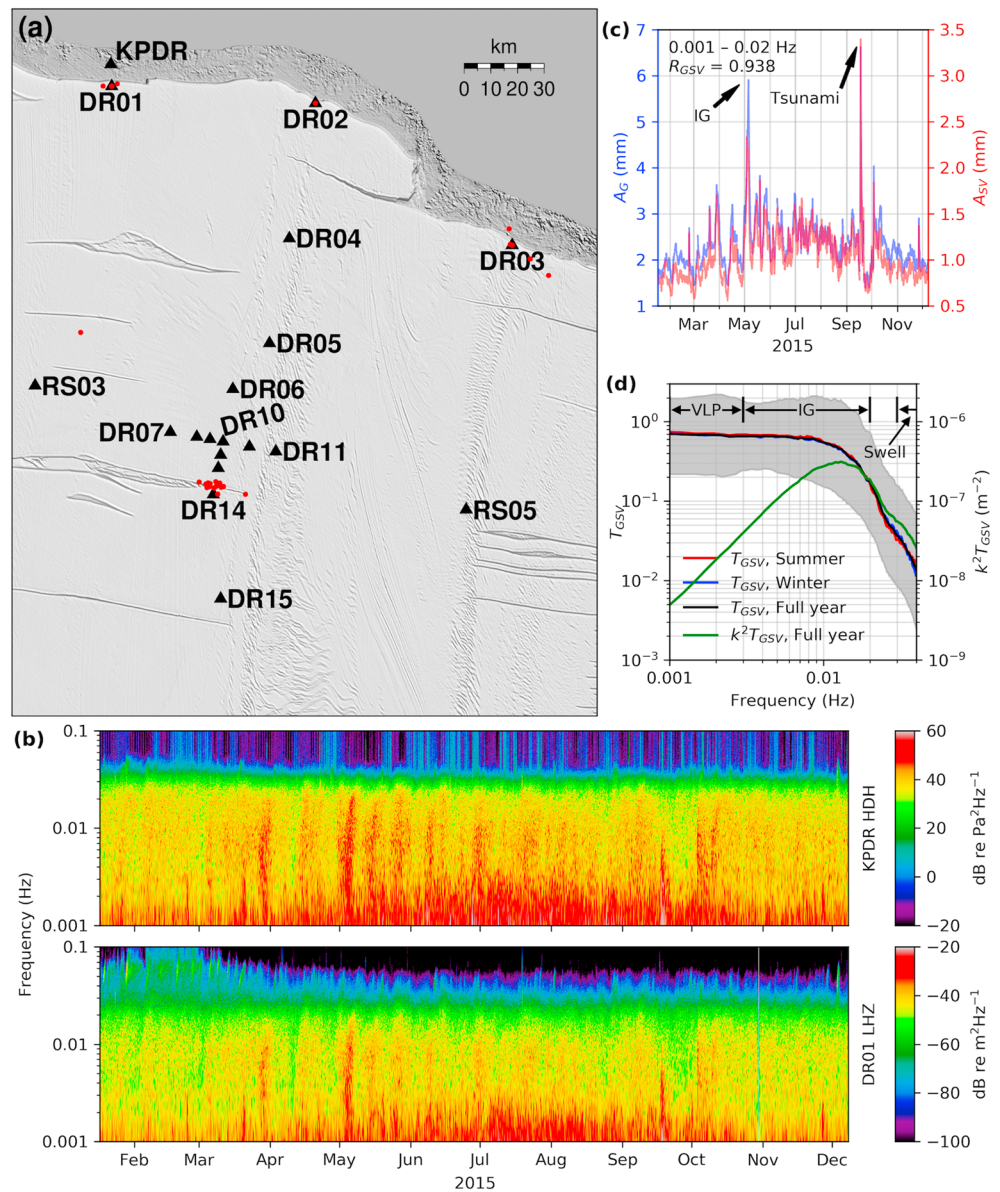


Figure 1. (a) On-ice broadband seismic stations and the near-front ocean bottom seismometer locations (triangles), with morphology as background (Haran et al., 2018), and located icequakes (red dots). (b) Spectrograms of the ocean bottom pressure at KPDR (top) and vertical displacement at DR01 (bottom). (c) Combined very long period (VLP) and infragravity (IG) band (0.001–0.02 Hz) A_G (blue) from KPDR near-front bottom pressure (b, top), compared with A_{SV} (red) from the vertical displacement at DR01 (b, bottom), each determined from integration over the VLP-IG band and smoothed with a 12-hr median filter, with major earthquakes and other strong transients removed (Text S1). The strong IG event in May and the tsunami in September (Bromirski et al., 2017) are indicated. (d) Summer (17 January to 15 March 2015, red), winter (1 July to 1 September 2015, blue), and full-year (17 January to 8 December 2015, black) $T_{GSV}(f)$, and full-year $k^2 T_{GSV}(f)$ (green) estimates. The gray area shows the range of the 5 to 95 percentiles of the 26,271 $T_{GSV}(f)$ realizations for full-year estimation.

(KPDR; Figure 1a) was deployed on the seafloor 8 km north of on-ice seismic station DR01 (6 km north of the shelf front) by the Korea Polar Research Institute from January to December 2015, sampled at 100 Hz. Pressure observations allow for the direct estimation of gravity wave amplitudes (A_G) near the RIS front. The concurrent deployment of seafloor pressure and nearby on-ice seismic stations enables simultaneous estimation of surface gravity wave amplitudes (A_G) and near-front vertical displacement amplitudes (A_{SV}). This allows for estimation of an empirical frequency-dependent ocean-wave-to-ice shelf displacement amplitude transfer function, $T_{GSV}(f)$.

Gravity wave forcing at the RIS covers a wide frequency/period range, from <10 s (local wind waves) to >300 s (tsunamis). The RIS response is characterized in the very long period (VLP; 0.001 – 0.003 Hz or $1,000$ – 300 s), IG (0.003 – 0.02 Hz or 30 – 50 s), and swell (0.03 – 0.1 Hz or 3 – 10 s) bands. The transition band (0.02 – 0.03 Hz or 5 – 30 s), which can include both IG and swell energy, is excluded. Dynamic pressure from surface gravity waves decays slowly with depth at low frequencies (<0.04 Hz), with significant signal reaching the seafloor at hydrophone KPDR (741 m) near the RIS front. Low-frequency gravity waves excite high-amplitude A_{SV} at nearby on-ice station DR01 (Figure 1b). Episodic strong IG arrivals are observed at both KPDR and DR01. These signals primarily originate from the nonlinear transformation of long-period swell in shallow water along the Pacific coasts of North, Central, and South America (Bromirski & Gerstoft, 2009; Bromirski et al., 2010; Herbers et al., 1995). IG events are associated with heightened levels in the VLP band, particularly during the austral winter from late March to early October. In contrast, swell excites high-amplitude A_{SV} at DR01 during the austral summer from December to March (Figure 1b).

The frequency-dependent gravity wave attenuation by sea ice contributes to seasonal variations of the amplitude of swell impacting the RIS. The wave amplitude A_G decays exponentially with distance, exponent proportional to f^n ($1.9 \leq n \leq 3.6$) (Meylan et al., 2018), indicating much faster attenuation at higher frequencies. In the austral winter, IG waves are minimally attenuated by sea ice (Bromirski et al., 2010, 2017), with high-frequency swell (0.04 – 0.1 Hz) significantly attenuated (Figure 1b).

Because ice fracturing is associated with rift propagation and iceberg calving, icequake activity is an indicator of changes in ice shelf integrity. The impact of gravity wave excitation on RIS integrity can be assessed in part by the temporal and spatial distribution of wave-induced icequake activity. Icequakes are generally classified by seismic source processes (Aster & Winberry, 2017). Rift icequakes are associated with crevasse extension, spanning the 5 – 50 Hz band (Bassis et al., 2007). Basal shear icequakes are associated with basal sliding over bedrock, causing stick-slip events (Wiens et al., 2008). Basal nonshear seismicity has rarely been observed and is hydrofracture-related (Podolskiy & Walter, 2016).

This study examines icequake activity across the RIS at 1 – 8 Hz, with rift and icefront icequake signals identified. Aspects of the importance of gravity wave forcing on RIS integrity can be inferred from the association of the spatial and temporal distribution of the icequakes with the seasonal variation of the gravity wave intensity.

2. Transfer Function $T_{GSV}(f)$

The magnitude of gravity wave-induced stresses on ice shelves that cause fracturing is a function of wave intensity and the ocean-to-ice shelf energy transfer. Due to the frequency-dependent hydrodynamic filtering, gravity wave signals can only be detected at KPDR (741-m depth) below ~ 0.04 Hz, above which the dynamic pressure is generally below the background noise. Therefore, the estimation of the ocean-wave-to-ice shelf displacement amplitude transfer function, $T_{GSV}(f)$, is constrained to VLP, IG, and low-frequency swell (0.03 – 0.04 Hz) bands.

Simultaneous VLP and IG arrivals observed at KPDR and DR01 are well correlated, with the full-year correlation coefficient $R_{GSV} = 0.938$ between A_G and A_{SV} over the combined VLP and IG bands (Figure 1c). Similarly, R_{GSV} is also high for low-frequency swell (annual $R_{GSV} = 0.916$). High R_{GSV} indicates that reliable estimates of $T_{GSV}(f)$ can be determined, providing an observation-based estimate of the gravity-wave/ice shelf response.

The summer (17 January to 15 March 2015), winter (1 July to 1 September 2015), and full-year (17 January to 8 December 2015) $T_{GSV}(f)$ were determined following the methodology in Text S1 in the supporting information, showing little seasonal variation below 0.04 Hz. The median full-year $T_{GSV}(f)$ (Figure 1d, black curve) has a narrow range 0.6 – 0.7 in the 0.001 - to 0.01 -Hz band, spanning the VLP band and part of the IG band. $T_{GSV}(f)$ does not approach unity at the low-frequency end, probably because A_G is overestimated due to nongravity-wave-induced signals included in the bottom pressure measurements, which reduces $T_{GSV}(f)$. The spectrum of the seafloor horizontal seismic displacement at KPDR is 10^3 to 10^4 higher than the vertical component over 0.001 – 0.04 Hz (Figure S1), consistent with tidal-current-generated contributions (Bromirski et al., 2005). $T_{GSV}(f)$ decreases by $\sim 97\%$ from 0.01 to 0.04 Hz, potentially because (1) frequency-dependent hydrodynamic filtering results in less energy reaching the ice shelf cavity to force ice shelf flexural vibrations (Chen et al., 2018) and/or (2) tidal current noise extends to these higher frequencies where A_G estimation is more sensitive to bottom pressure.

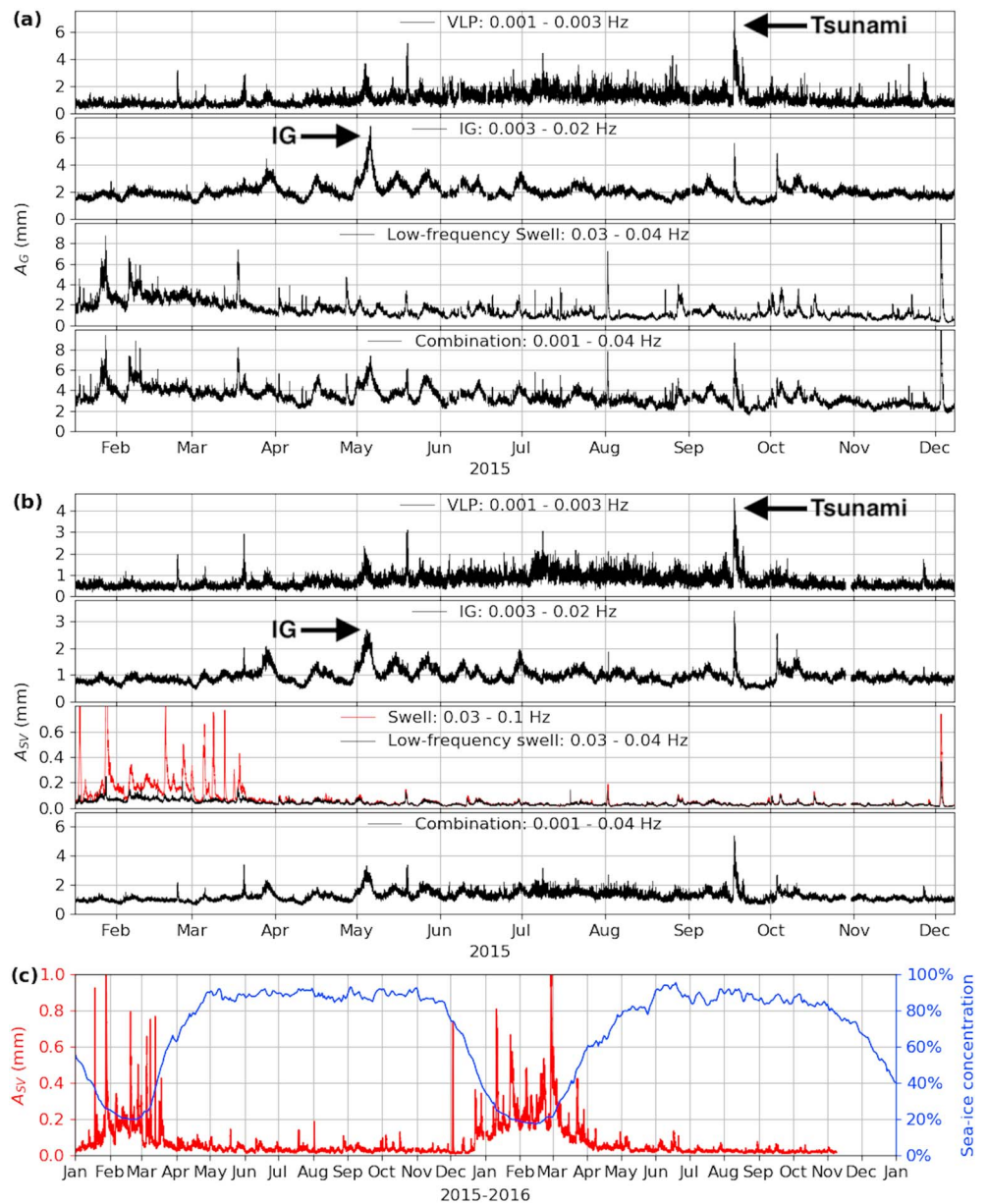


Figure 2. (a) A_G at KPDR estimated from bottom pressure, Figure 1b. Clipped amplitudes in early December are 13.2 and 13.5 mm for the 0.03- to 0.04- and 0.001- to 0.04-Hz bands. (b) A_{SV} at DR01. Amplitudes of the two off-scale 0.03- to 0.1-Hz peaks in January are 0.9 and 2.1 mm. (c) Swell-band A_{SV} (0.03–0.1 Hz, red) at DR01 and sea-ice concentration (blue) over the Ross Sea (Figure S2).

The extensional strain perturbation Σ induced by gravity wave impacts may be associated with ice fracturing. Assuming A_{SV} is primarily due to flexural waves, Σ is proportional to $k^2 A_{SV}$, where k is the wave number of the flexural waves (Lipovsky, 2018). The peak in the strain response is in the IG band (Figures 1d and S6). With $T_{GSV}(f)$ corrected, $k^2 T_{GSV}(f)$ can be used for Σ estimation, and association of incoming gravity waves with icequake activity.

3. A_G and A_{SV} in the VLP, IG, and Swell Bands

$T_{GSV}(f)$ variability motivates detailed comparisons of A_G (Figure 2a) and A_{SV} (Figure 2b) in the VLP, IG, and swell bands. Tsunami, strong IG, and swell signals are observed as high-amplitude short-duration events, in addition to the RIS response to seasonal variation of wave activity.

The VLP-band A_G and A_{SV} are higher in winter than in summer. Average VLP-band A_G is twice as large in winter (~ 2 mm) compared with summer (< 1 mm), reflecting heightened storm activity over the Southern Ocean in winter. Similarly, as $T_{GSV}(f)$ indicates, corresponding VLP-band A_{SV} in winter (~ 1 mm) is about twice that during summer (~ 0.5 mm). The highest VLP-band A_G (7 mm) and A_{SV} (4 mm) in 2015 are observed on 17–18 September, resulting from tsunami arrivals generated by the Mw 8.3 Chilean earthquake on 16 September. Tsunami-excited flexural-gravity waves were detected propagating southward across the RIS by the on-ice seismic array (Bromirski et al., 2017).

Though the background IG-band A_G (~ 2 mm) and A_{SV} (~ 1 mm) do not vary significantly with season, there are more strong IG arrivals in winter. The highest IG-band A_G in 2015 (7 mm) is observed in early May, when high A_{SV} (2.7 mm) and cross-ice shelf flexural-gravity waves were also observed (Bromirski et al., 2017), compared with the highest IG-band A_{SV} (3.3 mm) observed during the mid-September tsunami.

A_G was estimated for the low-frequency swell band, while A_{SV} is estimated for both the low-frequency swell band and full swell band (Figure 2). Unlike VLP, IG, and low-frequency swell, high-frequency swell is readily attenuated by sea ice. Consequently, A_{SV} is significantly higher in summer (2–8 mm) than in winter (1–4 mm, except for an 8-mm event). As swell attenuation by sea ice is very effective above 0.05 Hz, a strong seasonal variation of A_{SV} for the full swell band results, with amplitudes sporadically above 0.5 mm, and up to 2.1 mm in summer versus 0.02–0.2 mm in winter. The summer-winter seasonal transition occurs within 5–10 days during mid-March, when sea ice begins to form over the Ross Sea (Figures 2c and S2). Generally, $A_{SV} < 0.2$ mm for sea-ice concentration $> 50\%$ (sea ice covers > 700 km north of the RIS), except once in December 2015, due to a strong storm near the RIS (Movie S1).

To investigate the full RIS response, A_G and A_{SV} were calculated for the combined frequency band (0.001–0.04 Hz). A_G is slightly higher in summer than in winter, primarily due to less sea ice attenuation of swell near 0.04 Hz. In contrast, A_{SV} is higher in winter when more VLP and IG energy are produced by heightened storm activity.

4. Icequakes

We focus on RIS seismicity in the 1- to 8-Hz band, the dominant band of icequake energy. Icequakes were detected using STA/LTA methodology (Text S2; Withers et al., 1998), removing spurious transients and teleseismic signals. For spectral and statistical analyses, the 250 highest (waveform envelope) amplitude icequakes over the 2-year deployment were identified for each station. Their amplitude distributions, Figure 4e, show two icequake types, those near the shelf front and those interior RIS. Icequake signals at near-rift DR14 are the strongest nonicefront icequakes, but are typically a factor 10–100 lower in amplitude than icefront events.

The 20 highest-amplitude icequake signals at DR14 were located along nearby WR4 rift (Walker et al., 2013) (Figure 1a; Text S3 location methodology), consistent with a more complete catalog in Olinger et al. (2019). Though most icequakes near DR14 were observed at multiple stations and thus locatable, few icefront icequakes were detected at multiple stations due in part to seismic array spacing (Figure 1a). The locatable icequakes observed at DR01 (four), DR02 (one), and DR03 (eight) occurred near the icefront, potentially resulting from different mechanisms than rift icequakes near DR14. Rift icequakes cannot be observed over more than ~ 60 km (from DR14 to DR05), while higher-amplitude icefront icequakes are detectable 160 km away (from DR01 to DR14).

To investigate differences between rift and icefront icequakes, representative icequakes near DR14 and DR01 were selected, with seafloor KPDR (Figure 1a) providing additional information. Rift and icefront icequakes were characterized based on 0.1- to 20-Hz spectral content relative to their background noise levels (Figure 3). Seismic moveout speeds and particle motion characteristics differentiate the icequakes.

4.1. Rift Icequakes

At DR14, summer (15 January to 15 March 2015) and winter (1 July to 1 September 2015) background vertical displacement spectral levels are broadly similar, with summer < 10 dB higher in the 0.4- to 2-Hz band (Figure 3a), showing that the seasonal variation of ocean wave intensity and local environmental factors (e.g., temperature and wind) do not strongly affect background noise levels, and consequently will not affect year-round icequake detection. The 1- to 10-Hz median icequake spectrum for selected larger events is ~ 20 – 30 dB above the background.

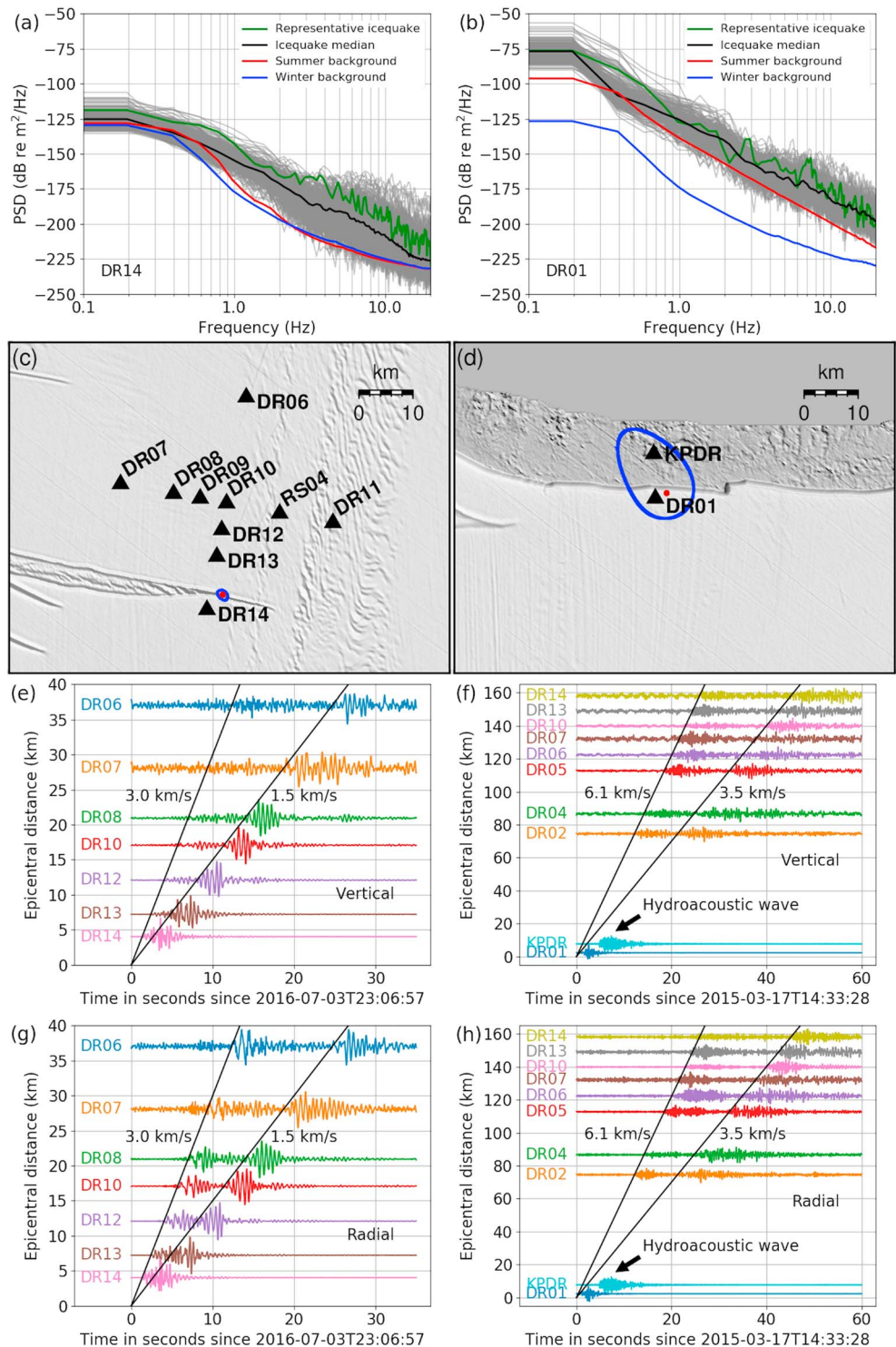


Figure 3. DR14 (a) and DR01 (b) vertical displacement spectra of the 250 strongest icequake signals (gray) with median (black) and representative icequake (green), including median summer (15 January to 15 March 2015, red) and winter (1 July to 1 September 2015, blue) background noise spectra. Station locations (black triangles) near DR14 (c) and near DR01 (d) with representative icequakes (red dots) indicated. Icequake location 95% confidence intervals (blue) and surface morphology (Haran et al., 2018) are shown. Icequakes were located using phase moveout speeds of 3.0 km/s (c, DR14) and 6.1 km/s (d, DR01). Vertical (e) and radial (g) displacement moveout of representative icequake near DR14, 2–8 Hz bandpassed and normalized to its maximum amplitude. (f and h) Same as (e) and (g) but for DR01, with KPDR pressure response included.

The representative rift icequake is located on rift WR4 north of DR14 (Figure 3c). Two major phases are observed in projections on the vertical-radial plane. The first phase has a moveout speed of 3.0 km/s (Figures 3e and 3g) and is strongest on the radial component. The second phase has a moveout speed of 1.5 km/s and is observed on both vertical and horizontal components with retrograde elliptical polarization (Movie S2). Synthetic seismograms on the ice shelf surface (Figure S3) show extensional and flexural Lamb wave speeds of 3.0 and 1.5 km/s (flexural Lamb waves degenerate to Rayleigh waves above 4 Hz), respectively, similar to the observed moveout speeds (Figures 3e and 3g).

4.2. Icefront Icequakes

At DR01, the median winter background spectrum is similar to DR14, while the summer background spectrum is 20–30 dB higher than winter (Figure 3b), suggesting that icefront background noise results primarily from seasonal variations in sea ice attenuation of ocean wave energy. The median icequake spectrum is 10–20 dB higher than the summer background spectrum over most of the 0.1- to 20-Hz band.

The representative icefront icequake is located near DR01 at the icefront (Figure 3d). Two major phases are observed, with moveout speeds of 6.1 and 3.5 km/s (Figures 3f and 3h). The moveout speed of the first phase is much higher than the ice P wave speed estimated with dispersion analysis (3.77 km/s; Diez et al., 2016); therefore, it must have traveled through the upper crust. The second phase travels close to ice P wave speed but has comparable vertical and radial components (Movie S3), different from the radial-dominant extensional Lamb waves observed for rift icequakes. Modeling suggests that the slower phase is likely extensional Lamb waves generated by a source with primarily vertical forcing (Figure S3), resulting in relatively smaller horizontal motions. Alternatively, propagation through semilithified seafloor sediments (P wave speed 3.75 km/s; Peters et al., 2008), is a possibility. This icequake is also observed at KPDR, with moveout speed of 1.6 km/s (near 1.5 km/s ocean acoustic wave speed) over the estimated 9-km epicentral distance. Similar icefront icequakes likely result from either iceberg calving, intrashelf fracturing, or possibly basal crevasse expansion near the icefront. Icequake observations at DR01 and KPDR indicate such events are common. Among the 50 strongest icequake signals when both DR01 and KPDR were deployed, 23 icequakes were clearly detected at both stations, including the two locatable events in 2015.

5. Discussion

Icequake occurrence and distribution can be indicative of changes in ice shelf integrity. Rift and icefront icequakes have different temporal distributions. Most icefront icequakes occur in summer and early fall. Among the 250 strongest icequake signals at DR01, DR02, and DR03 and 236, 243, and 205 occurred from January to March, respectively, the same period when sea ice is minimal and full-swell-band icefront vibrations are strongest (Figures 4a–4c and S4). The rapid increase (January) and decrease (March) of full-swell-band vibrations are accompanied by a change in cryoseismicity (Figure S4), indicating an association of swell and ice fracturing at the icefront. Sea ice efficiently attenuates swell, with most strong swell impacts at the RIS front observed during low sea-ice concentrations (<50%; Figure 2c). Interestingly, the winter collapses of the Larsen A and B and Wilkins ice shelves were preceded by greater prevalence and frequency of low sea-ice concentration (Massom et al., 2018). These observations are consistent with swell contributing to ice fracturing.

$T_{GSV}(f)$ is much larger in VLP band than in the low-frequency swell band (Figure 1d), and likely the full swell band as well. Thus, lower-amplitude VLP waves can excite similar ice shelf responses as much higher-amplitude swell. For example, 4.3-cm VLP waves can excite 2.6-cm A_{SV} , while 2-m swell (0.04 Hz) is needed, with correspondingly higher swell at higher frequencies. Thwaites Ice Shelf, which has thickness and bathymetry similar to RIS (Figure S5), should respond similarly.

Although there appears to be a clear association between full-band swell forcing and icefront cryoseismicity, icequakes do not always occur during strong swell arrivals. However, about 70% of the strong icequakes detected during summer 2015 at DR01 occurred during swell events. Additionally, three icequake swarms occurred at DR01 in summer 2015 and two at DR02 in February 2016 (Figure S4), with each swarm associated with strong swell arrivals. Fewer icequakes were observed in 2016 than in 2015 regardless of the swarms, although El Niño occurring in early 2016 caused stronger swell impacts at the RIS (Figures 4a–4d, blue curves). At DR03, 149 strong icequakes were detected between 1 December 2014 and 1 September 2015, while only 100 icequakes were detected during the El Niño. Because the peak strain response occurs in the IG

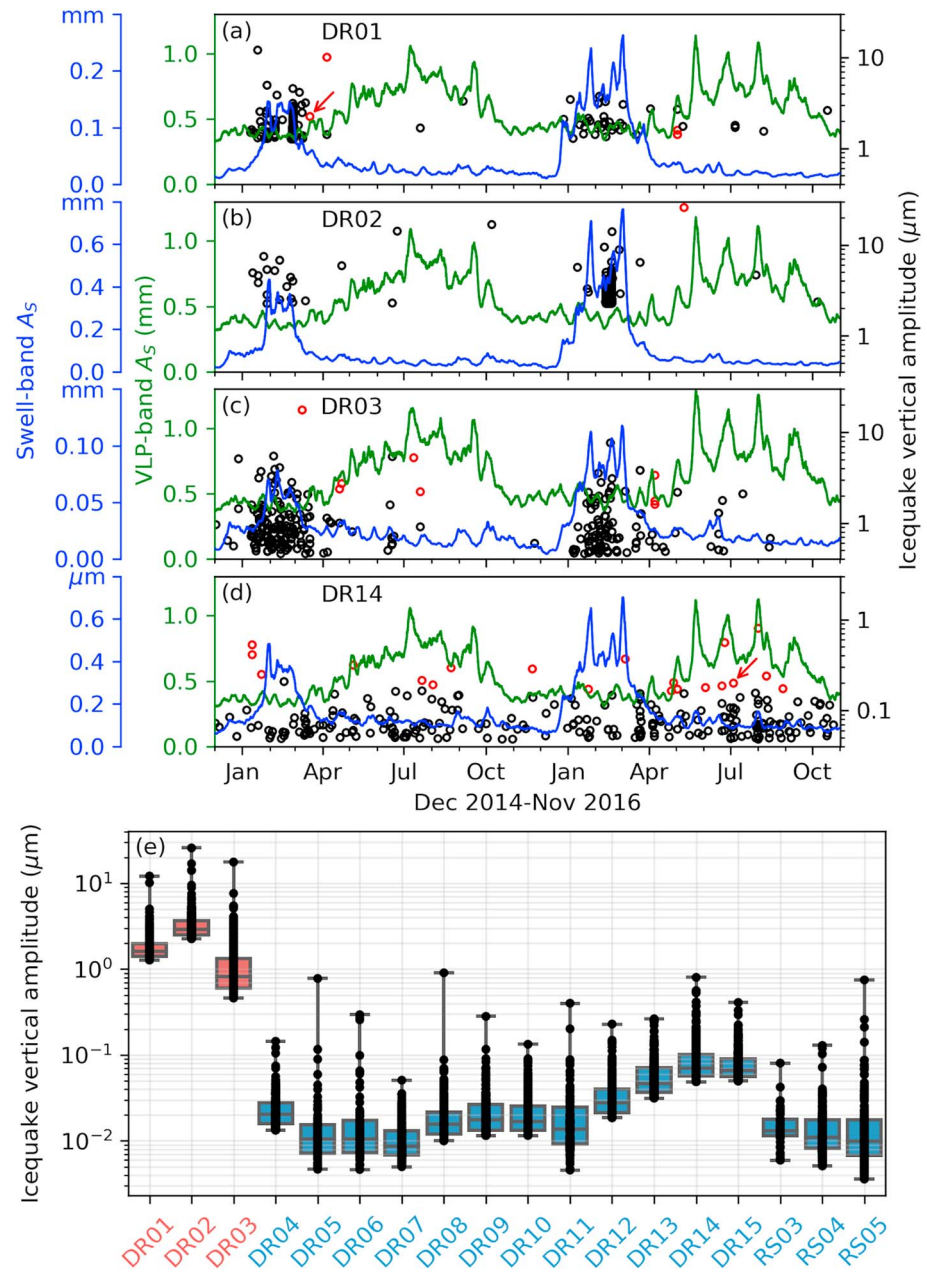


Figure 4. DR01 (a), DR02 (b), DR03 (c), and DR14 (d) weekly medians of A_{SV} in the very long period (VLP) band (0.001–0.003 Hz, green curve) and swell band (0.03–0.1 Hz, blue curve), with the temporal distribution of the 250 strongest icequake signals (red circles: located in Figure 1a; black circles: unlocated) from 1 December 2014 to 1 November 2016. Representative icequakes near DR01 and DR14 in Figure 3 are indicated by arrows in (a) and (d). Swell-band A_{SV} units are mm for DR01, DR02, and DR03, but micrometers for DR14. (e) Vertical amplitude range of the strongest 250 (or fewer) icequake signals (dots) at each station in Figure 1a. Boxes and interior bands indicate the quartiles. Fewer than 250 icequakes were detected at DR05 (80), DR06 (83), DR11 (106), RS03 (41), RS04 (214), and RS05 (203).

band (Figure 1d), this suggests that persistent IG and swell forcing, which commonly occur simultaneously, contribute to fracture expansion and fatigue weakening that predisposes the ice shelf for icefront seismicity.

In contrast to icefront icequakes, seasonal variation of rift seismicity is not as strong. Slightly more strong rift icequakes occurred in winter and early spring, the same period when VLP is strongest. Among the 250 strongest icequake signals at DR14, on average, ~ 14 occurred per month from June to September (Figure 4d) versus 9 in other months. This low seasonal variation suggests a lack of direct correlation between rift

icequakes and VLP intensity. However, persistent VLP forcing, which is unaffected by sea ice in winter and minimally attenuated across the ice shelf (Bromirski et al., 2017), may facilitate icequakes indirectly. Additionally, rift icequakes have been associated with thermal and tidally driven stresses in a more extensive study of the rift seismicity (Olinger et al., 2019), indicating that multiple factors are involved.

The spatial distribution of strong icequake detections across the RIS is influenced by the array configuration and station positions (Figure 1a). Icefront stations (all located 2 km from the ice edge) show amplitude variability (Figure 4e) that must be associated with gravity wave variability along the front and/or variable ice integrity. Near-rift amplitudes generally decrease with epicentral distance from the rift near DR14. At stations away from the rift or front (RS03, DR05, DR06, and DR11), strong icequake detections are far fewer and with lower amplitude, indicating that there are regions of the RIS that exhibit relatively low seismicity, even in passive ice regions (Fürst et al., 2016) where ice velocity is high (Rignot et al., 2011).

6. Conclusions

Ocean gravity wave impacts may cause ice fracturing and weaken ice shelf integrity. Estimation of gravity wave amplitudes, A_G , from seafloor pressure data acquired near the RIS front, together with on-ice vertical seismic displacement amplitudes, A_{SV} , at a near-front seismic station, allows determination of the ocean-to-ice shelf (A_G -to- A_{SV}) transfer function, $T_{GSV}(f)$, giving a mechanical link between ocean forcing and ice shelf responses.

Rift and icefront icequakes were observed on the RIS, both exhibiting two arrivals. Rift seismicity does not show strong correlation with gravity wave intensity. Icefront icequakes span a wider frequency band with higher moveout speeds, indicating travel paths through the upper crust. These may result from iceberg calving, intrashelf fracturing, or basal crevasse expansion. Icefront seismicity has a strong seasonal variation, with most events occurring during the austral summer when sea ice is absent and swell-shelf interaction is strong. However, strong swell, IG, or VLP arrivals are not always associated with particular icefront icequake occurrences, suggesting that cumulative effects from gravity waves cause fatigue weakening that facilitates the observed fracturing.

Acknowledgments

Bromirski, Gerstoft, and Chen were supported by NSF grant PLR-1246151. Bromirski also received support from NSF grant OPP-1744856 and CAL-DPR-C1670002. Stephen, Wiens, Aster, and Nyblade were supported under NSF grants PLR-1246416, 1142518, 1141916, and 1142126, respectively. Lee and Yun were supported by a research grant from the Korean Ministry of Oceans and Fisheries (KIMST20190361; PM19020). Seismic instruments and on-ice support were provided by the Incorporated Research Institutions for Seismology (IRIS) through the PASSCAL Instrument Center at New Mexico Tech. The RIS and KPDR seismic data are archived at the IRIS Data Management Center, <http://ds.iris.edu/ds/nodes/dmc/>, with network codes XH and KP, respectively. The facilities of the IRIS Consortium are supported by the National Science Foundation under Cooperative Agreement EAR-1261681 and the DOE National Nuclear Security Administration. We thank Patrick Shore, Michael Baker, Cai Chen, Robert Anthony, Reinhard Flick, Jerry Wanetick, Weisen Shen, Tsitsi Madziwa Nussinov, and Laura Stevens for their help with field operations. Logistical support from the U.S. Antarctica Program and staff at McMurdo Station was critical and is much appreciated.

References

- Aster, R. C., & Winberry, J. P. (2017). Glacial seismology. *Reports on Progress in Physics*, 80(12), 126801. <https://doi.org/10.1088/1361-6633/aa8473>
- Bassis, J. N., Fricker, H. A., Coleman, R., Bock, Y., Behrens, J., Darnell, D., et al. (2007). Seismicity and deformation associated with ice-shelf rift propagation. *Journal of Glaciology*, 53(183), 523–536. <https://doi.org/10.3189/002214307784409207>
- Bassis, J. N., Fricker, H. A., Coleman, R., & Minster, J.-B. (2008). An investigation into the forces that drive ice-shelf rift propagation on the Amery Ice Shelf, East Antarctica. *Journal of Glaciology*, 54(184), 17–27. <https://doi.org/10.3189/002214308784409116>
- Bromirski, P. D., Chen, Z., Stephen, R. A., Gerstoft, P., Arcas, D., Diez, A., et al. (2017). Tsunami and infragravity waves impacting Antarctic ice shelves. *Journal of Geophysical Research: Oceans*, 122, 5786–5801. <https://doi.org/10.1002/2017JC012913>
- Bromirski, P. D., Diez, A., Gerstoft, P., Stephen, R. A., Bolmer, T., Wiens, D. A., et al. (2015). Ross Ice Shelf vibrations. *Geophysical Research Letters*, 42, 7589–7597. <https://doi.org/10.1002/2015GL065284>
- Bromirski, P. D., Duennebie, F. K., & Stephen, R. A. (2005). Mid-ocean microseisms. *Geochemistry, Geophysics, Geosystems*, 6, Q04009. <https://doi.org/10.1029/2004GC000768>
- Bromirski, P. D., & Gerstoft, P. (2009). Dominant source regions of the Earth's "hum" are coastal. *Geophysical Research Letters*, 36, L13303. <https://doi.org/10.1029/2009GL038903>
- Bromirski, P. D., Sergienko, O. V., & MacAyeal, D. R. (2010). Transoceanic infragravity waves impacting Antarctic ice shelves. *Geophysical Research Letters*, 37, L02502. <https://doi.org/10.1029/2009GL041488>
- Bruno, K. M., Okal, E. A., & MacAyeal, D. R. (2011). Antarctic ice-shelf calving triggered by the Honshu (Japan) earthquake and tsunami, March 2011. *Journal of Glaciology*, 57(205), 785–788. <https://doi.org/10.3189/002214311798043681>
- Chen, Z., Bromirski, P. D., Gerstoft, P., Stephen, R. A., Wiens, D. A., Aster, R. C., & Nyblade, A. A. (2018). Ocean-excited plate waves in the Ross and Pine Island Glacier ice shelves. *Journal of Glaciology*, 64(247), 730–744. <https://doi.org/10.1017/jog.2018.66>
- Diez, A., Bromirski, P., Gerstoft, P., Stephen, R., Anthony, R., Aster, R., et al. (2016). Ice shelf structure derived from dispersion curve analysis of ambient seismic noise, Ross Ice Shelf, Antarctica. *Geophysical Journal International*, 205(2), 785–795. <https://doi.org/10.1093/gji/ggw036>
- Fürst, J. J., Durand, G., Gillet-Chaulet, F., Tavard, L., Rankl, M., Braun, M., & Gagliardini, O. (2016). The safety band of Antarctic ice shelves. *Nature Climate Change*, 6, 479–482. <https://doi.org/10.1038/nclimate2912>
- Fox, C., & Squire, V. A. (1991). Coupling between the ocean and an ice shelf. *Annals of Glaciology*, 15, 101–108. <https://doi.org/10.3189/1991AoG15-1-101-108>
- Haran, T., Klinger, M., Bohlander, J., Fahnestock, M., Painter, T., & Scambos, T. (2018). *MEaSURES MODIS Mosaic of Antarctica 2013–2014 (MOA2014) Image Map, Version 1*. Boulder, CO: NSIDC: National Snow and Ice Data Center. <https://doi.org/10.5067/RNF17BP824UM>
- Herbers, T. H. C., Elgar, S., & Guza, R. T. (1995). Generation and propagation of infragravity waves. *Journal of Geophysical Research*, 100, 24,863–24,872. <https://doi.org/10.1029/95JC02680>

- Ilyas, M., Meylan, M. H., Lamichhane, B., & Bennetts, L. G. (2018). Time-domain and modal response of ice shelves to wave forcing using the finite element method. *Journal of Fluids and Structures*, 80, 113–131. <https://doi.org/10.1016/j.jfluidstructs.2018.03.010>
- Lipovsky, B. P. (2018). Ice shelf rift propagation and the mechanics of wave-induced fracture. *Journal of Geophysical Research: Oceans*, 123, 4014–4033. <https://doi.org/10.1029/2017JC013664>
- MacAyeal, D. R. (1987). Ice-shelf backpressure: Form drag versus dynamic drag. In C. J. Van der Veen & J. Oerlemans (Eds.), *Dynamics of the West Antarctic Ice Sheet* (pp. 141–160). Dordrecht, Netherlands: Springer.
- Massom, R. A., Scambos, T. A., Bennetts, L. G., Reid, P., Squire, V. A., & Stammerjohn, S. E. (2018). Antarctic ice shelf disintegration triggered by sea ice loss and ocean swell. *Nature*, 558(7710), 383–389. <https://doi.org/10.1038/s41586-018-0212-1>
- Meylan, M. H., Bennetts, L. G., Mosig, J. E. M., Rogers, W. E., Doble, M. J., & Peter, M. A. (2018). Dispersion relations, power laws, and energy loss for waves in the marginal ice zone. *Journal of Geophysical Research: Oceans*, 123, 3322–3335. <https://doi.org/10.1002/2018JC013776>
- Olinger, S., Wiens, D. A., Lipovsky, B. P., Aster, R. C., Nyblade, A. A., Stephen, R. A., et al. (2019). Tidal and thermal stresses drive seismicity along a major Ross Ice Shelf rift. *Geophysical Research Letters*, 46, 6644–6652. <https://doi.org/10.1029/2019GL082842>
- Papathanasiou, T. K., Karperaki, A. E., & Belibassakis, K. A. (2019). On the resonant hydroelastic behaviour of ice shelves. *Ocean Modelling*, 133, 11–26. <https://doi.org/10.1016/j.ocemod.2018.10.008>
- Peters, L. E., Anandakrishnan, S., Holland, C. W., Horgan, H. J., Blankenship, D. D., & Voigt, D. E. (2008). Seismic detection of a subglacial lake near the South Pole, Antarctica. *Geophysical Research Letters*, 35, L23501. <https://doi.org/10.1029/2008GL035704>
- Podolskiy, E. A., & Walter, F. (2016). Cryoseismology. *Reviews of Geophysics*, 54, 708–758. <https://doi.org/10.1002/2016RG000526>
- Press, F., & Ewing, M. (1951). Propagation of elastic waves in a floating ice sheet. *Eos, Transactions American Geophysical Union*, 32, 673–678. <https://doi.org/10.1029/TR032i005p00673>
- Rignot, E., Casassa, G., Gogineni, P., Krabill, W., Rivera, A., & Thomas, R. (2004). Accelerated ice discharge from the Antarctic Peninsula following the collapse of Larsen B ice shelf. *Geophysical Research Letters*, 31, L18401. <https://doi.org/10.1029/2004GL020697>
- Rignot, E., Mouginot, J., & Scheuchl, B. (2011). Ice flow of the Antarctic ice sheet. *Science*, 333(6048), 1427–1430. <https://doi.org/10.1126/science.1208336>
- Scambos, T. A., Bohlander, J. A., Shuman, C. A., & Skvarca, P. (2004). Glacier acceleration and thinning after ice shelf collapse in the Larsen B embayment, Antarctica. *Geophysical Research Letters*, 31, L18402. <https://doi.org/10.1029/2004GL020670>
- Scambos, T. A., Hulbe, C., Fahnestock, M., & Bohlander, J. (2000). The link between climate warming and break-up of ice shelves in the Antarctic Peninsula. *Journal of Glaciology*, 46(154), 516–530. <https://doi.org/10.3189/172756500781833043>
- Sergienko, O. V. (2010). Elastic response of floating glacier ice to impact of long-period ocean waves. *Journal of Geophysical Research*, 115, F04028. <https://doi.org/10.1029/2010JF001721>
- Sergienko, O. V. (2017). Behavior of flexural gravity waves on ice shelves: Application to the Ross Ice Shelf. *Journal of Geophysical Research: Oceans*, 122, 6147–6164. <https://doi.org/10.1002/2017JC012947>
- Walker, C. C., Bassis, J. N., Fricker, H. A., & Czerwinski, R. J. (2013). Structural and environmental controls on Antarctic ice shelf rift propagation inferred from satellite monitoring. *Journal of Geophysical Research: Earth Surface*, 118, 2354–2364. <https://doi.org/10.1002/2013JF002742>
- Wiens, D. A., Anandakrishnan, S., Winberry, J. Paul, & King, M. A. (2008). Simultaneous teleseismic and geodetic observations of the stick-slip motion of an Antarctic ice stream. *Nature*, 453, 770–774. <https://doi.org/10.1038/nature06990>
- Withers, M., Aster, R., Young, C., Beiriger, J., Harris, M., Moore, S., & Trujillo, J. (1998). A comparison of select trigger algorithms for automated global seismic phase and event detection. *Bulletin of the Seismological Society of America*, 88(1), 95–106.

Erratum

In the originally published version of this article, there were errors published in the Discussion section. These errors have since been corrected and the present version may be considered the authoritative version of record.